

Influence of cavity and magnetic confinements on the signal enhancement and plasma parameters of laser-induced Mg and Ti plasmas

Research Article

Cite this article: Asamoah E, Xia Y, Hongbing Y, Wei P, Jiawei C, Weihua Z, Lin Z, Quaisie JK (2020). Influence of cavity and magnetic confinements on the signal enhancement and plasma parameters of laser-induced Mg and Ti plasmas. *Laser and Particle Beams* **38**, 61–72. <https://doi.org/10.1017/S0263034620000014>


Received: 13 August 2019
Revised: 23 September 2019
Accepted: 8 January 2020
First published online: 10 February 2020

Key words:

Cavity confinement; electron density; electron temperature; emission enhancement; LIBS; magnetic confinement; Mg spectra

Authors for correspondence:

Emmanuel Asamoah, School of Mechanical Engineering, Jiangsu University, Zhenjiang, Jiangsu 212013, China.
E-mail: asamoah_grace@hotmail.com;
Yao Hongbing, College of Science, Hohai University, Nanjing, Jiangsu 210098, China. Email: alenyao@hhu.edu.cn

Emmanuel Asamoah¹ , Ye Xia¹, Yao Hongbing², Pengyu Wei³, Cong Jiawei¹, Zhu Weihua², Zhang Lin² and James Kwasi Quaisie¹

¹School of Mechanical Engineering, Jiangsu University, Zhenjiang, Jiangsu 212013, China; ²College of Science, Hohai University, Nanjing, Jiangsu 210098, China and ³China Ship Scientific Research Center, Wuxi, Jiangsu 214082, China

Abstract

In this study, we have spectroscopically investigated the plasma generated by a Q-switched Nd:YAG laser operating at its fundamental wavelength of 1064 nm focused on magnesium (Mg) and titanium (Ti) target samples in the air under atmospheric pressure. We employed circular cavities of radii (2.5, 3.0, and 3.5 mm) and a square cavity to investigate the cavity confinement effect on the spectral emission intensities of the plasmas. We observed that the circular cavity of radius 2.5 mm had the maximum signal enhancement, and this can be attributed to the compression of the plasma and reheating by the reflected shock waves. The maximum enhancement factor of the Mg I-518.4 nm line was reached at approximately 3.8, 3.4, and 2.8 with a circular cavity of radius 2.5, 3.0, and 3.5 mm, respectively, at a delay time of 350 ns and a laser energy of 350 mJ. By applying varying external magnetic fields (0.47, 0.62, 0.91, and 1.23 T) across the generated plasma, the plasma parameters such as electron temperature and number density have been investigated. From our results, we observed that the radius of the cavity had a tremendous effect on the enhancement of the emission signal intensities. We also found that the increase in the electron temperature and the number density can be attributed to the increase in the applied magnetic field and the laser energy. From our calculations, the value of β , which was less than 1 for all the cases, confirms that there was a plasma confinement at the presence of the magnetic field.

Introduction

Laser-induced breakdown spectroscopy (LIBS) is an analytical technique (Zhang *et al.*, 1999) that uses a laser to generate plasma from the target samples. The method is focusing a high power laser on a small surface area of the target sample (Popov *et al.*, 2014; Choi *et al.*, 2016; Shaheen *et al.*, 2016), which then ablates the surface to generate the plasma. The emitted radiations from the plasma are collected and processed to attain the quantitative and qualitative data on the target sample elemental composition. LIBS has been employed in a vast number of applications such as forensics (Bridge *et al.*, 2007; Naes *et al.*, 2008; Rodriguez-Celis *et al.*, 2008), pharmaceuticals (Asimellis *et al.*, 2005), military and security (Harmon *et al.*, 2006; Gottfried *et al.*, 2008), environmental analyses (Corsi *et al.*, 2002; Lei *et al.*, 2009; Boueri *et al.*, 2011), archeological analyses (Müller and Stege, 2003; Carmona *et al.*, 2005; Giakoumaki *et al.*, 2007), and material processing (Awan *et al.*, 2013; Sun *et al.*, 2015; Li *et al.*, 2018; Markiewicz-Keszycka *et al.*, 2018). The LIBS technique has gained an unprecedented attention from scientist all over the world from plasma physics, chemical physics, and material sciences (Neogi and Thareja, 1999), due to its ability for *in situ* analysis, little or no sample preparation, fast and remote detection, and multi-elemental diagnosis. This technique can also be utilized to analyze all forms of matter irrespective of its physical state from solids (Sturm *et al.*, 2000), liquids (Michel *et al.*, 2007), and gases (Cremers and Radziemski, 1983; Radziemski and Cremers, 1989; Lee *et al.*, 1997; Sturm and Noll, 2003). LIBS offers more advantages over other spectroscopic techniques such as mass spectroscopy, the electrode spark, and the inductively coupled plasma (Amoruso *et al.*, 1999). One of the significant challenges of LIBS is its low sensitivity, in spite of the advantages of the LIBS technique. Over the past decades to improve the LIBS sensitivity, numerous papers on the enhancement of the signal sensitivity of the LIBS technique have been reported using either cavity or magnetic confinement (Popov *et al.*, 2009). Research has been published (Guo *et al.*, 2011) on the study of combined spatial and magnetic confinements using both permanent magnets and hemispherical cavity in the LIBS for Co and Cr metallic samples.

Guo *et al.* (2013) have studied the accuracy of quantitative analysis improvement of low concentration elements of a laser-induced steel plasma confined in a cavity using an Nd:YAG laser in the air. They investigated several elements with low concentrations, such as vanadium (V), chromium (Cr), and manganese (Mn). A significant enhancement in the emission intensities of the elements such as V, Cr, and Mn was observed, with an enhancement factor of 4.2, 3.1, and 2.97, respectively. Their results predicted that the accuracy of quantitative analysis by spatial confinement was improved.

Shao *et al.* (2017) also employed a Q-switched Nd:YAG laser to investigate the effect of the cylindrical cavity height on the laser-induced silicon plasmas. They reported that the enhancement of the spectra intensity of Si (I) 390.55 nm was dependent on the height of the cylindrical cavity. The maximum enhancement factor was recorded to be approximately 8.3 with a cylindrical cavity of height 6 mm.

Bashir *et al.* (2012) presented a work on the influence of the magnetic field on laser-ablated Mg-alloy plasma parameters along with surface structuring under different ambient conditions of Ar, Ne, and He at various irradiances ranging from 0.3 to 2.6 GW/cm² at fixed pressure of 5 Torr.

Dawood *et al.* (2018) also employed an Nd:YAG laser to study the effect of the magnetic field on the plasma parameters and the surface modification of laser-induced Cu plasma. They found that the plasma parameters of the Cu plasma are more enhanced in the presence of the magnetic field as compared with the field-free case. They reported that the enhancement was a result of magnetic confinement, Joule heating confinement, and adiabatic compression.

In this work, we report on a laser-induced plasma generated by an Nd:YAG laser operating at its fundamental wavelength of 1064 nm under atmospheric pressure. The main goals of this work are to study:

- The influence of the magnetic field on the spectral intensities and the plasma parameters of the Mg and Ti plasmas and
- The enhancement of the emission signal intensities of the Mg plasma by utilizing different circular cavity radii and shape for the confinement of the LIBS.

Experimental procedure

The schematic diagram of the experimental setup is represented in Figure 1a. The experiment was conducted in air under atmospheric pressure. A Q-switched Nd:YAG laser operating at its fundamental wavelength of 1064 nm, with a pulse width of 10 ns, and the repetition rate of 10 Hz was used to ablate the surface of the Mg-target sample (certified purity of 99.99%) to generate the plasma plume. A quartz lens with a focal length of 150 mm was used to focus the laser beam on the surface of the Mg target. We employed laser energies of 200, 300, and 400 mJ, which were measured by a pyrometric detector.

The emission spectra from the laser-induced plasmas were collected by a fiber bundle (50- μ m core diameter) coupled with a Michelle spectrometer with an inbuilt intensified charged coupled device (ICCD) camera (1024 \times 1024 pixels, iStar from Andor Technology). The delay generator (Stanford Research System, model DG645) was utilized to vary the time between the laser pulse and the acquisition of the spectral images. Two different shapes of the columnar cavity were employed for the confinement. The square cavity of side 7 mm (half of the side as

3.5 mm, denoted by R_s , 3.5 mm) and a circular cavity with three different radii of 2.5, 3.0, and 3.5 mm (indicated by R_c , 2.5, 3.0, and 3.5 mm, respectively) were used in the experiment as depicted in Figure 1b. The depth of all the cavities was 7 mm. The cavity was tightly fitted to the 3D translation stage to ensure that the laser beam was focused at the center of the cavity. The data acquisition and its analysis were performed with a computer running a manufacturer software (Andor Solis, Andor Technology).

The schematic diagram in Figure 2 is also used to study the magnetic confinement of the laser-induced plasma. The target samples were mounted on an adjustable holder, which was sandwiched between two permanent magnets. The distance between the two magnets was kept constant. The Gauss meter was then used to measure the magnetic field strength of the magnets. The magnetic fields produced by the magnets were utilized in a way that the magnetic field lines were perpendicular to the plasma expansion.

Results and discussion

Cavity confinement

Spectral intensities

The time-integrated laser-induced spectra of the Mg plasma were measured to investigate the influence of the cavity confinement on the signal enhancement of the plasma. The emission spectra of the magnesium plasma recorded with circular cavities with three different radii at the laser energy of 250 mJ were obtained in the spectral ranges of 515.8–519.4 nm, as shown in Figure 3. The Nd:YAG laser beam was focused to a spot size of approximately 0.42 mm in diameter, with a laser energy of 250 mJ and a delay time of 350 ns. The acquisitions of the spectra data were recorded a suitable number of accumulations to increase the signal-to-noise ratio. The emission intensities of the Mg atomic lines were all enhanced in the presence of the circular cavity. The atomic lines of the Mg spectra lines were used from the data compiled from the National Institute for Standards and Technology database (NIST).

Effect of the cavity radii and shape on the plasma

To improve the cavity dimension in this study, we employed the circular cavities of different radii. The emission intensities of the Mg plasma were studied using circular cavities of radii 2.5, 3.0, and 3.5 mm, respectively, as shown in Figure 4. The intensities of the different circular cavity radii were plotted with the cavity-free case (without cavity) for comparison. Comparing the emission intensities of the circular cavity of 2.5 mm radius with the cavity-free case (without cavity), the emission intensity of the Mg I-518.4 nm was slightly enhanced at a delay time of 50 ns. Increasing the delay time to 150 ns, the emission intensity started rising slowly and then increased significantly at a delay time of 200 ns, and this can be as a result of a decrease in the lifetime of the upper state of the Mg plasma due to the confinement. Afterwards, there was a rapid rise in the intensity of the circular cavity of 2.5 mm from 200 to 350 ns. Moreover, the emission intensity then decreases quickly after 350 ns. The highest enhancement of the 2.5 mm cavity radius was found to be approximately 3.8 at a delay time of 350 ns. Similar observations were obtained for the circular cavities of radii 3.0 and 3.5 mm and both obtained their maximum emission intensities at a delay time of 350 ns, reaching an enhancement factor of approximately 3.4 and 2.8, respectively. Comparing all the cavity radii with the

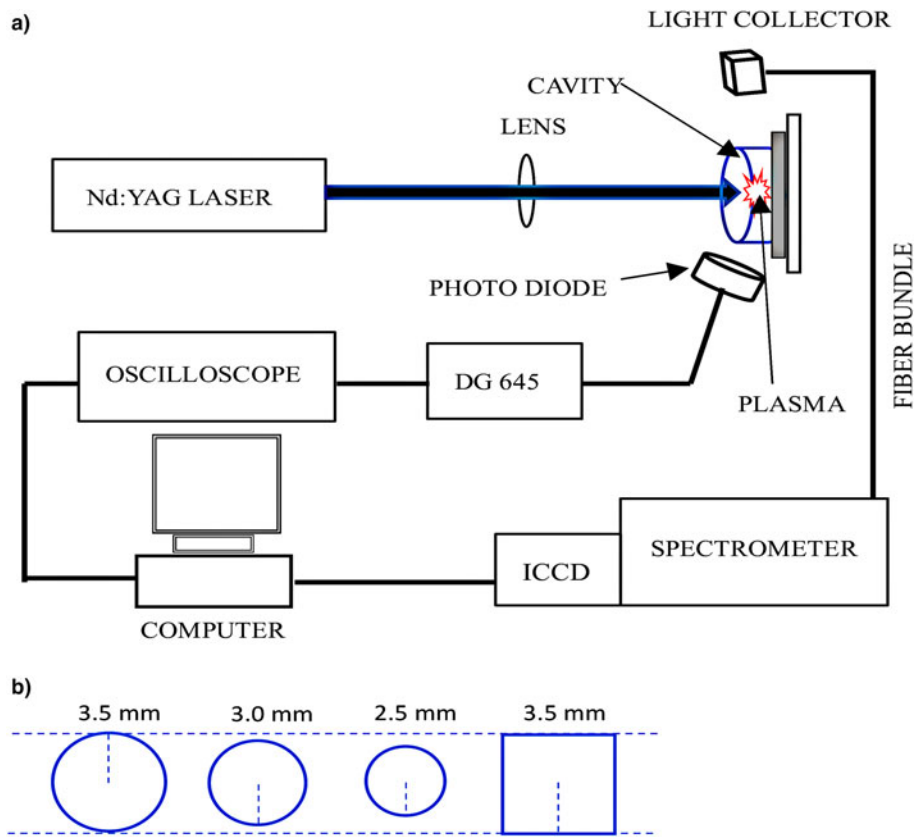


Fig. 1. (a) The schematic diagram of the experiment of the cavity confinement of the laser-induced Mg plasma. (b) Three different circular cavities with radii of 2.5, 3.0, and 3.5 mm and a square cavity with half of its side as 3.5 mm.

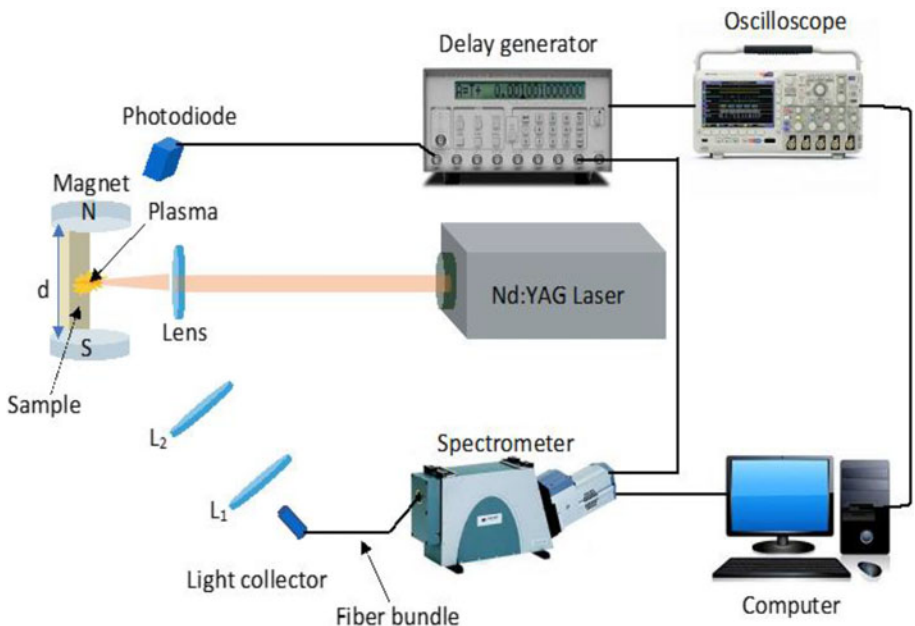


Fig. 2. The schematic diagram of the magnetic confinement of the laser-induced plasma at the atmospheric pressure.

cavity-free case (without cavity) as can be seen from Figure 4, the spectral intensities of all the three different cavity confinements were all enhanced. These enhancements resulted from the plasma compression, caused by the shock waves reflected from the walls of the cavities. The enhancement shows that the reflected shock waves have more effect on the Mg plasma plume (Gao *et al.*, 2015; Wang *et al.*, 2018). This is because the compression by

the shock wave would lead to an increase in the rate of collision between the particles, causing a rise in the number of atoms in high-energy states and thus reheating and keeping a higher temperature within the plasma plume, thereby causing an enhancement in the emission intensity of the Mg plasma (Guo *et al.*, 2013).

We observed that at a delay time of 350 ns, the size of the ablated plasma was compressed by the reflected shock wave,

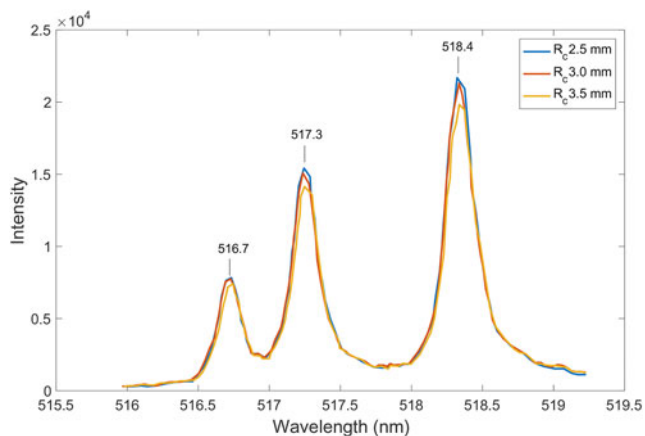


Fig. 3. The spectra for different circular cavities of radii (2.5, 3.0, and 3.5 mm) at a delay time of 350 ns and a laser energy of 250 mJ from the spectral range of 515.98–519.32 nm.

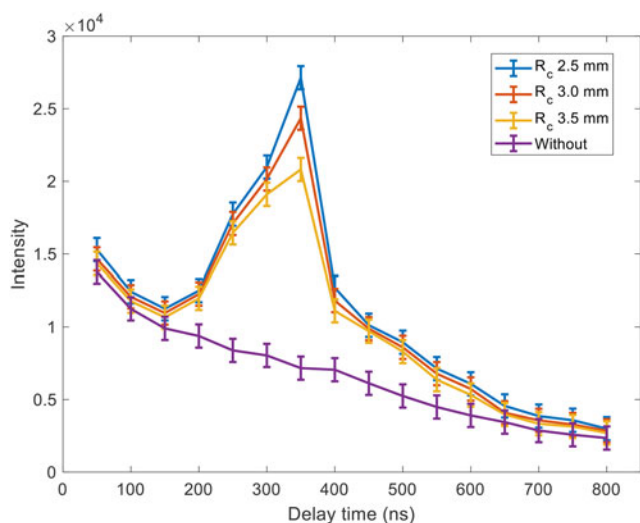


Fig. 4. Time-resolved spectroscopy of Mg I-518.4 nm with different circular cavity radii of 2.5, 3.0, and 3.5 mm and cavity-free case (without cavity) at a laser energy of 350 mJ.

thereby decreasing the size of the plasma. As a result, the maximum plasma density was attained. With a further increase in the delay time, the compression of the shock wave becomes weaker, and the shock wave propagates through the plasma. When this happens, the volume of the plasma expands; the plasma density then progressively decreases, leading to a decrease in the intensity of the plasma (Wang *et al.*, 2018).

From our results, we observed that the radius of the cavity had a tremendous effect on the enhancement of the emission intensities, and the circular cavity of radius 2.5 mm had the best confinement.

The spectral peak intensities of Mg I-516.7 nm, Mg I-517.3 nm, and Mg I-518.4 nm with different circular cavities of radii (2.5, 3.0, and 3.5 mm) at a delay time of 350 ns and a laser energy of 300 mJ are depicted in Figure 5. At a delay time of 350 ns and a laser energy of 300 mJ, the peak intensities of the Mg spectral lines confined with a circular cavity of radius 2.5 mm had the strongest emission intensity. We observed that the enhancement factors of the spectral intensities of the Mg

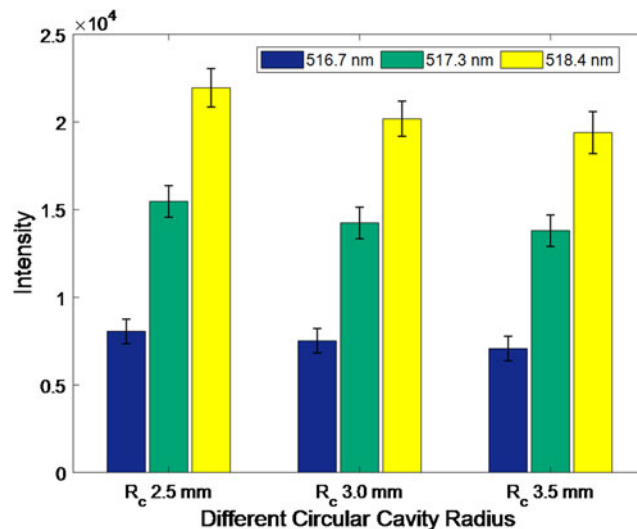


Fig. 5. The spectral peak intensities for different circular cavity radii (2.5, 3.0, and 3.5 mm) at a delay time of 350 ns and a laser energy of 300 mJ of Mg I-516.7 nm, Mg I-517.3 nm, and Mg I-518.4 nm.

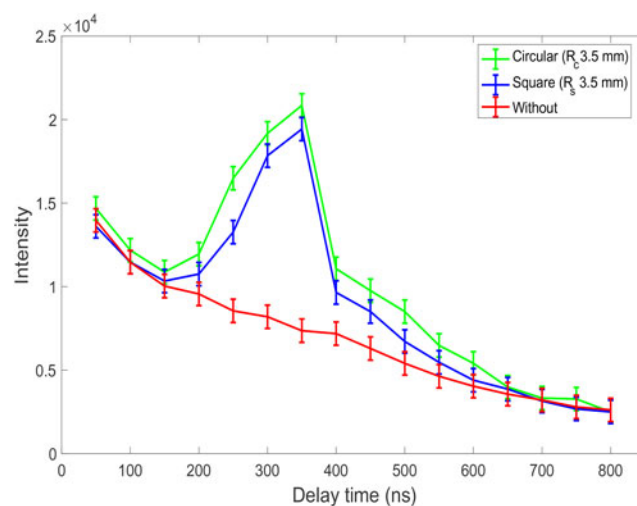


Fig. 6. The emission intensity of Mg plasma confined with a circular cavity of radius 3.5 mm (R_c 3.5 mm) and a square cavity of half of its side as 3.5 mm (R_s 3.5 mm) with different delay time at a laser energy of 250 mJ.

I-516.7 nm, Mg I-517.3 nm, and Mg I-518.4 nm spectral lines are higher with the circular cavity of radius 2.5 mm followed by the cavity radius of 3.0 and 3.5 mm.

A graph of a circular cavity with a radius 3.5 mm and a square cavity with the length of the side as 7 mm (half of its side as 3.5 mm) is shown in Figure 6. Comparing the square cavity with the cavity-free case (without cavity), we observed a general trend of decreasing spectral intensities with an increasing delay time from 50 to 800 ns with the cavity-free case (without cavity). From the graph in Figure 6, there was no significant increase in the spectral intensities of the square cavity with an increasing delay time from 50 to 150 ns as compared with the cavity-free case (without cavity). The intensities of the square cavity started to increase slowly from a delay time of 200 ns and then increased rapidly to its maximum intensity at a delay time of 350 ns. With a further increase in the delay time to 400 ns, the intensity then

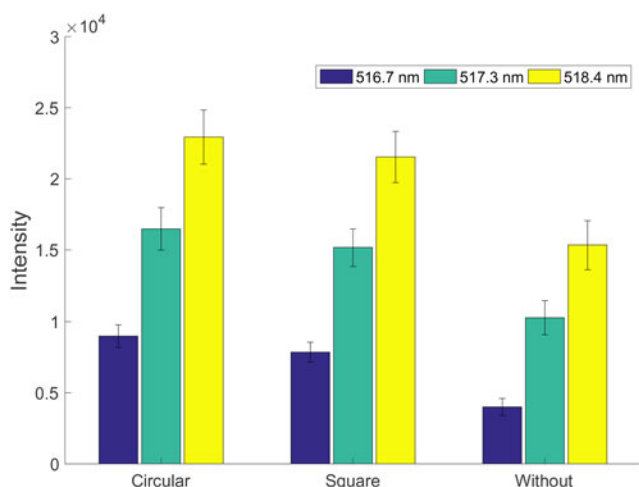


Fig. 7. The spectral peak intensities for the circular cavity of radius 3.5 mm, a square cavity with half of its side as 3.5 mm, and the cavity-free case (without cavity) at a delay time of 300 ns and a laser energy of 250 mJ of Mg I-516.7 nm, MgI-517.3 nm, and Mg I-518.4 nm.

drops sharply with increasing the delay time from 450 to 800 ns. Also, the intensity of the circular cavity was more enhanced as compared with the square cavity. The circular cavity attained its highest spectral intensity at a delay time of 350 ns and then decreased rapidly from a delay time of 400–700 ns. There was a slight increase in the intensity of the circular cavity from the delay time of 700–750 ns and then dropped again at a delay time of 800 ns.

Figure 7 shows the spectral peak intensities of Mg plasma confined with a circular cavity of radius 3.5 mm and a square cavity with half of its side as 3.5 mm at a delay time of 300 ns and a laser energy of 250 mJ with the Mg spectral lines of 516.7, 517.3, and 518.4 nm. The Mg I-518.4 nm attained the highest spectral peak intensity of 22,996. With the same laser energy and delay time, the spectral peak intensity of the square cavity was recorded as 21,578. Also, the cavity-free case (without cavity) recorded the lowest spectral peak intensity of the Mg I-518.4 nm as 15,267 at a delay time of 300 ns and a laser energy of 250 mJ. We observed that the peak intensities of the circular cavity are higher as compared with the square cavity and the cavity-free case (without cavity).

Determination of plasma temperature using the Boltzmann plot method

The electron temperature was obtained by employing the Boltzmann plot method (Aguilera and Aragón, 2004; Zhang et al., 2014; Hongbing et al., 2018), which can be expressed as follows:

$$\ln\left(\frac{I_{mn}\lambda_{mn}}{A_{mn}g_{mn}}\right) = -\frac{E_m}{k_B T} + \ln\left(\frac{hcN}{U(T)}\right) \tag{1}$$

where $U(T)$ is the partition function, the subscripts m and n represent the upper energy level of the transition and the lower energy level of the transition, respectively, c is the speed of light (ms^{-1}), E_m is the energy of the upper energy level (eV), k_B is

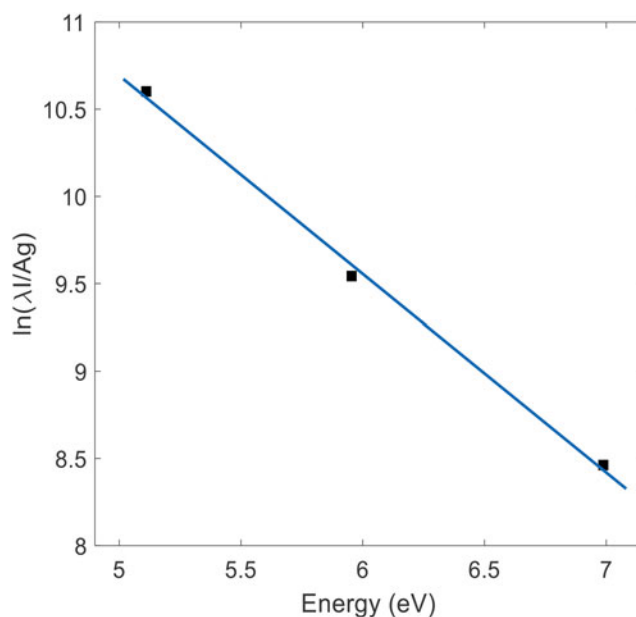


Fig. 8. The Boltzmann plot using Mg lines at a delay time of 350 ns and a laser energy of 250 mJ.

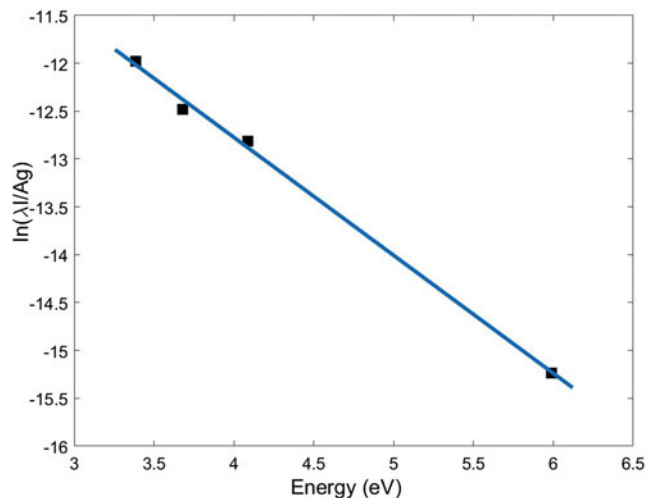


Fig. 9. The Saha Boltzmann plot using Ti lines at a delay time of 350 ns and a laser energy of 250 mJ.

the Boltzmann’s constant (eV K^{-1}), g_m is the statistical weight of the upper energy level, λ_{mn} is the transition wavelength (m), h is the Planck’s constant, N is the number density (m^{-3}), A_{mn} is the transition probability (s^{-1}), and T is the electron temperature (K) (Ahmed et al., 2017; Figures 8–10).

Plotting the energies of the upper energy levels (E_m) at the right-hand side of Eq. (1) against $\ln(I_{mn}\lambda_{mn}/A_{mn}g_{mn})$ at the left-hand side yields a linear plot with slope equal to $-1/k_B T$. By utilizing the atomic spectral lines of Mg I of wavelength 383.2, 470.3, and 518.4 nm, from the temperature can be deduced from the Boltzmann plot using the slope obtained from the plot. The spectroscopic parameters of both the Mg and Ti spectra lines retrieved from the NIST database are shown in Table 1.

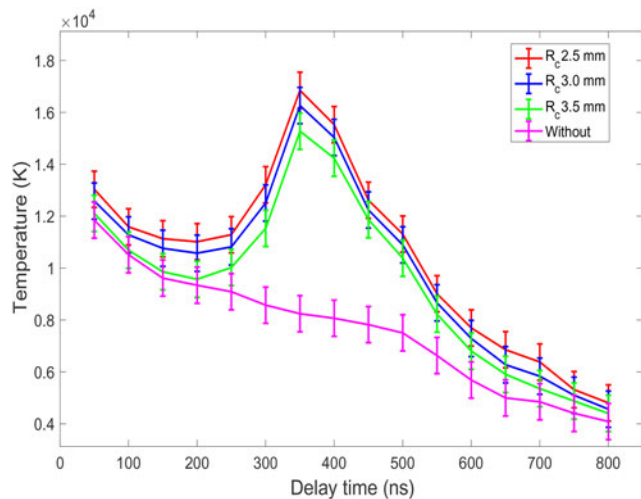


Fig. 10. The temporal evolution of the electron temperature of the Mg plasma, with different circular cavities (R_c 2.5, 3.0, and 3.5 mm) and the cavity-free case (without cavity) at a laser energy of 300 mJ.

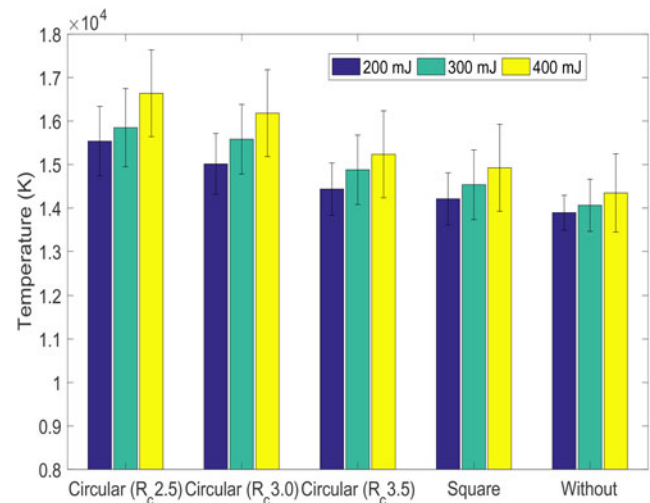


Fig. 11. The plot of the electron temperature at a delay time of 350 ns with different laser energies (200, 300, and 400 mJ) against the circular cavities (R_c 2.5, 3.0, and 3.5 mm), the square cavity, and the cavity-free case (without cavity).

Table 1. The spectroscopic data of Mg and Ti spectral lines obtained from the NIST database

Spectra line	λ_{mn} (nm)	E_m (eV)	A_{mn} ($\times 10^8 s^{-1}$)	g_m
Mg I	383.0	5.95	0.90	3
Mg I	383.2	5.95	1.21	5
Mg I	470.3	6.98	0.22	5
Mg I	516.7	5.11	0.11	3
Mg I	517.3	5.11	0.34	3
Mg I	518.4	5.11	0.56	3
Mg II	448.1	11.63	2.33	8
Ti I	336.2	5.99	1.58	9
Ti I	390.1	3.20	0.01	7
Ti I	430.1	3.72	0.16	7
Ti II	337.3	1.41	3.69	8
Ti II	368.5	3.97	0.0	6
Ti II	376.0	3.90	0.94	8
Ti II	376.2	5.89	0.22	8
Ti II	439.4	4.04	0.01	4
Ti II	450.1	3.87	0.09	6

Influence of the cavity radii on the electron temperature

The slope of the plot for the cavity-free case (without cavity) yielded an electron temperature of 7423 K at a delay time of 200 ns and a laser energy of 300 mJ. With the same laser energy and delay time, the electron temperature of the circular cavities of radii 2.5, 3.0, and 3.5 mm was recorded at 9188, 8575, and 7683 K, respectively. Comparing the plot of the electron temperature against the delay time, we observed that the electron temperature of the cavity-free case (without cavity) decreases with increasing delay time, and this result agrees with our previous work (Asamoah and Hongbing, 2017). But, with the circular cavity of radius 2.5 mm, the electron temperature does not follow the

usual trend, it started decreasing with increasing delay time from 50 to 200 ns and then began to rise slowly from 250 ns until it attained its highest electron temperature of 15,889 K at a delay time of 350 ns. It then starts to decrease from 400 to 800 ns. The circular cavity of radii 3.0 and 3.5 mm also obtained their highest electron temperatures as 14,843 and 13,833 K, respectively, at a delay time of 350 ns. The cavity confinement had a significant impact on the electron temperature with an enhancement factor of approximately 3.1, 2.6, and 2.3 with circular cavities of radii 2.5, 3.0, and 3.5 mm, respectively.

We also studied the temporal evolution of the electron temperature with three different laser energies (200, 300, and 400 mJ). The results of this study are depicted in Figure 11. We observed that at a delay time of 350 ns and a laser energy of 400 mJ, the circular cavity of radius 2.5 mm had the maximum electron temperature of 16,853 K. The square cavity also obtained its maximum electron temperature of 15,018 K at a delay time of 350 ns and a laser energy of 400 mJ. From Figure 11, it can be seen that the electron temperature increases with increasing laser energy, with the circular cavity of radius 2.5 mm having the highest electron temperature.

We further employed a laser energy of 500 mJ to study the temporal evolution of the electron temperature. At a delay time of 350 ns, the electron temperatures of the Mg plasma for the circular cavities of radii 2.5, 3.0, and 3.5 mm were recorded as 18,920, 18,325, and 17,408 K, respectively. The electron temperature increased significantly by increasing the laser energy to 500 mJ as shown in Figure 12. The significant enhancement of the electron temperature occurred between the delay time of 200 and 350 ns. From Figure 13, the electron temperature decreases rapidly with an increasing delay time from 350 to 750 ns with a laser energy of 500 mJ.

Magnetic confinement

The emission spectra of the Mg and Ti target samples are investigated with and without magnetic fields at several delay times. Figures 14 and 15 depict time-resolved Mg and Ti emission spectra at delay time from 0 to 35 μs , respectively. From Figure 14, the

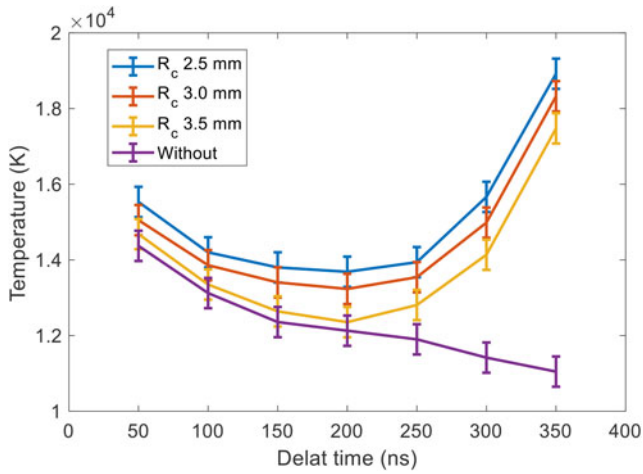


Fig. 12. The temporal evolution of the electron temperature of the Mg plasma, with different circular cavities (R_c 2.5 mm, 3.0 mm, and 3.5 mm) and the cavity-free case (without cavity) from the delay time of 50–350 ns with a laser energy of 500 mJ.

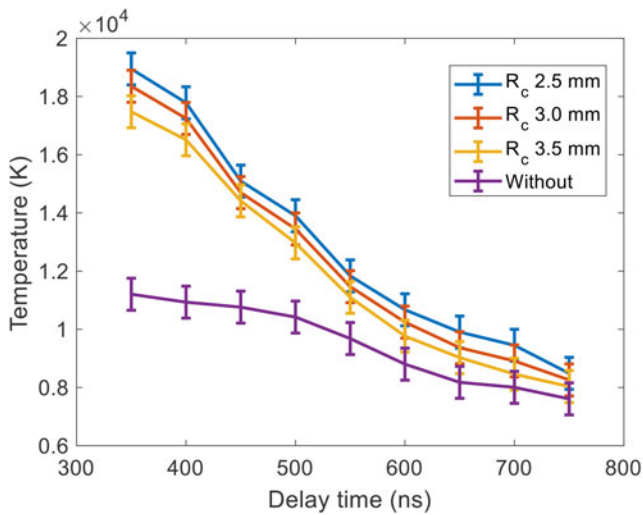


Fig. 13. The temporal evolution of the electron temperature of the Mg plasma, with different circular cavities (R_c 2.5 mm, 3.0 mm, and 3.5 mm) and the cavity-free case (without cavity) from the delay time of 350–750 ns with a laser energy of 500 mJ.

Mg spectra of Mg I-518.4 nm attained the highest spectral intensity of 8927.95. We also observed a drop in the spectral intensities of the Mg lines with increasing delay time. Figure 15 also shows the Ti spectra for both the atomic lines of Ti I: 336.2, 390.1, and 430.1 nm and the ionic lines of Ti II: 337.3, 368.5, 376.2, and 439.5 nm. The Ti II-376.2 nm spectral line reached its maximum spectral intensity at 4569.86 with a delay time of 5 μ s at the presence of the magnetic field of 0.47 T. The Mg I-518.4 nm spectral line was fitted to the Lorentz profile in Figure 16, with a laser energy of 50 mJ and a delay time of 25 μ s.

The enhancements of the spectral intensities of the laser-induced plasmas are attributed to the magnetic confinement effect. By applying external magnetic fields, the Lorentz force would significantly influence the ions and electrons within the produced plasmas, thereby reducing the propagation of the ablated plume. Also, other phenomena are introduced at the presence of the applied magnetic field such as the conversion of kinetic energy into plasma thermal energy and plume

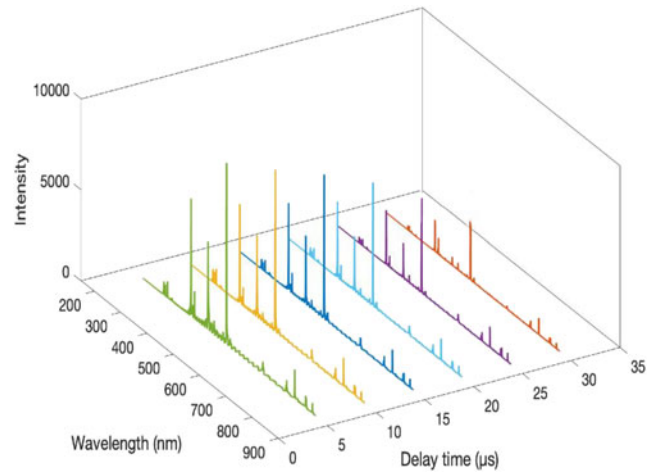


Fig. 14. Time-resolved emission spectrum of Mg-induced plasma at several delay times in the spectral region of 200–865 nm with a laser energy of 50 mJ at the presence of a magnetic field of 0.47 T.

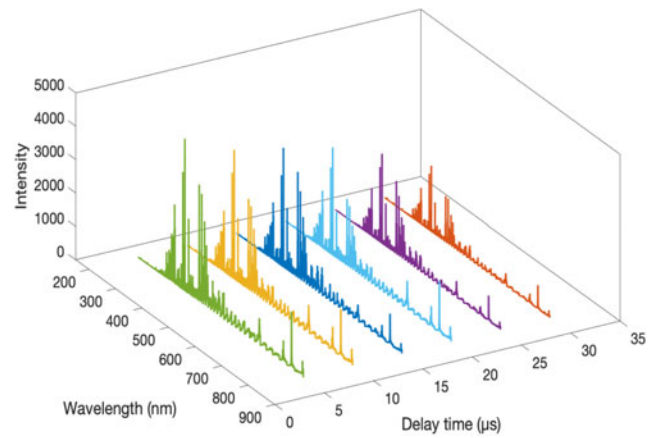


Fig. 15. Time-resolved emission spectrum of Ti-induced plasma at several delay times in the spectral region of 300–562 nm with a laser energy of 50 mJ at the presence of a magnetic field of 0.47 T.

confinement. However, the magnetic field cannot entirely stop the propagation of the ablated plume; hence, the ablated plume propagates slowly through the magnetic field (Joshi *et al.*, 2010; Iftikhar *et al.*, 2017). Using the magnetohydrodynamic equation, the parameter β can be deduced by the following equation (Harilal *et al.*, 2004; Shen *et al.*, 2006):

$$\beta = \frac{8\pi n_e k_B T_e}{B^2} = \frac{\text{Plasma pressure}}{\text{Magnetic pressure}} \quad (2)$$

where T_e , n_e , and k_B are the electron temperature, number density, and Boltzmann constant, respectively, β is the ratio of the plasma pressure and the magnetic pressure, and B is the magnetic field strength (Rai *et al.*, 1998; Iftikhar *et al.*, 2017). At the presence of the magnetic field, the deceleration of the ablated plasma expansion can be expressed as follows:

$$\frac{v_2}{v_1} = \left(1 - \frac{1}{\beta}\right)^{(1/2)} \quad (3)$$

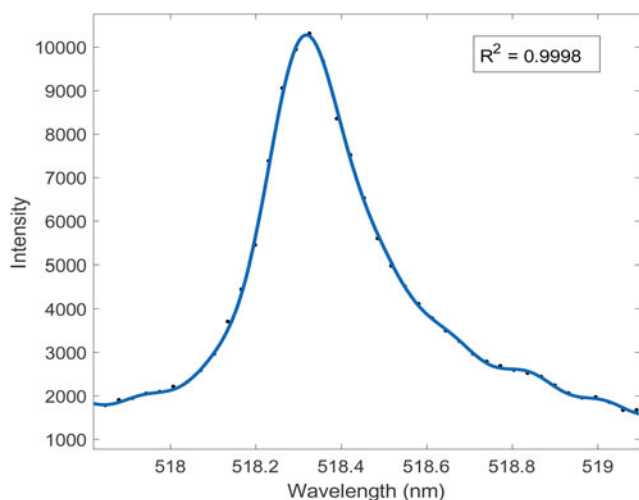


Fig. 16. The Lorentz fit of the Mg I-518.4 nm line with a delay time of 25 μs and a laser energy of 50 mJ at the presence of a magnetic field of 0.47 T.

where v_2 and v_1 represent the asymptotic plasma expansion velocity with and without a magnetic field, respectively. When $\beta = 1$, the ablated plasma would be stopped entirely by the magnetic field; this shows that the magnetic pressure is equal to the thermal pressure. If $\beta > 1$, the magnetic confinement would be ineffective. However, if $\beta < 1$, then magnetic confinement becomes effective (Shen *et al.*, 2006; Iftikhar *et al.*, 2017; Akhtar *et al.*, 2019). From all the calculations of β in all the cases, we found that the value of β was less than 1, which confirms that there was plasma confinement at the presence of the magnetic field.

Employing a magnetic field of 1.23 T and a laser energy 450 mJ in Figure 17, the Mg I-518.4 nm spectral line intensity increases from a delay time of 1–4 μs . We observed the highest intensity of the Mg I-518.4 nm spectra at 23,880 with a delay time of 4 μs . The intensity then drops tremendously from a delay time of 5–32 μs . The magnetic field of 0.62 and 0.91 T also attained their maximum intensities at a delay time of 2 μs and then decreased from the delay time of 3–32 μs . Also, reducing the magnetic field strength to 0.47 T, the intensity of the Mg I-518.4 nm line reached its maximum intensity at a delay time of 4 μs and then decreased.

For the Ti II-376.2 nm spectra lines in Figure 18, the maximum spectral intensity was reached at the delay time of 2 μs at the presence of the magnetic field 1.23 T. The Ti II-376.2 nm spectra lines also had a decreasing trend with an increasing delay time from 4 to 32 μs .

Plotting the spectral intensities of both the Mg and Ti plasmas against the laser energies is represented in Figures 19 and 20, respectively. The intensities of the Mg plasma in Figure 19 increased with an increasing laser energy from 50 to 350 mJ at the presence and absence of the magnetic field of 0, 0.47, 0.62, 0.91, and 1.23 T. Also, from Figure 20, the spectral intensities of the Ti plasma predicted a general trend of increasing intensities with increasing laser energy at the presence and absence of the magnetic fields.

Saha-Boltzmann plot method

Considering the ionic and the neutral lines of the Ti spectra, the Saha-Boltzmann plot method can be employed to determine the plasma temperatures of the laser-induced Ti plasmas. The

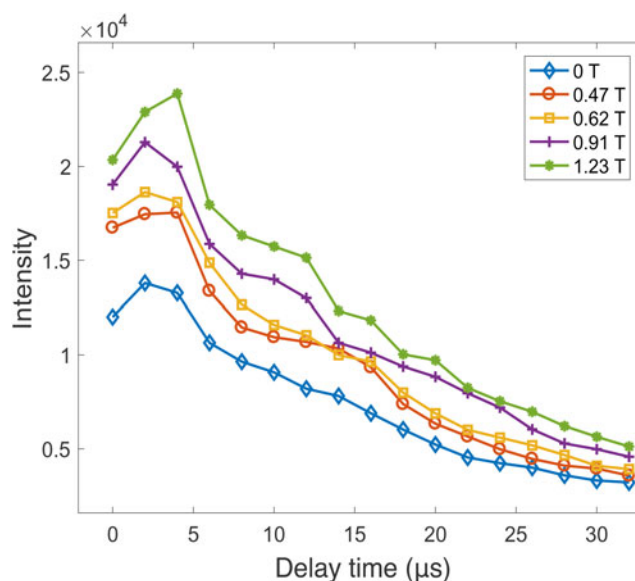


Fig. 17. The intensities of the Mg I-518.4 nm spectra line against the delay times, with a laser energy of 450 mJ at the presence and absence of the magnetic field.

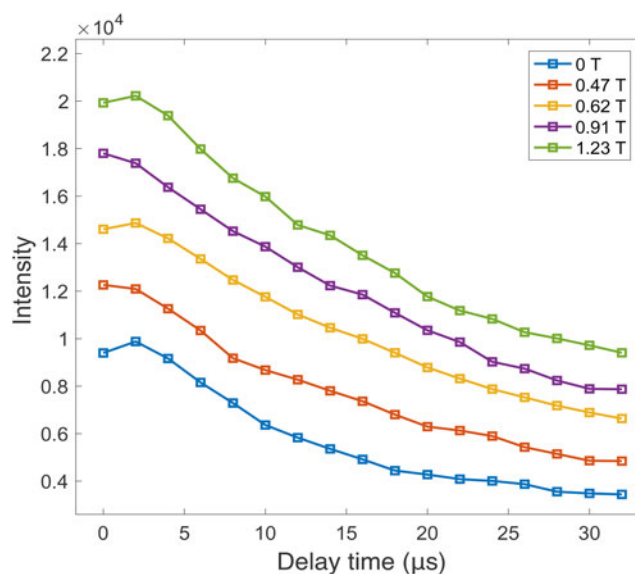


Fig. 18. The intensities of the Ti II-376.2 nm spectra line against the delay times, with a laser energy of 450 mJ at the presence and absence of the magnetic field.

neutral and the ionic lines can be expressed in Eqs. (4) and (5), respectively:

$$\ln\left(\frac{I_1\lambda_1}{g_1A_1}\right) = -\frac{1}{kT}E_k^1 + \ln\left(\frac{hc}{Z_0(T)}\frac{N_0}{Z_0(T)}\right) \quad (4)$$

$$\begin{aligned} \ln\left(\frac{I_2\lambda_2}{g_2A_2}\right) - \ln\left(\frac{2(2\pi mk)(3/2)T^{3/2}}{h^3}\frac{T^{3/2}}{N_e}\right) \\ = -\frac{1}{kT} \times (E_k^2 + E_{IP}) + \ln\left(\frac{hc}{Z_0(T)}\frac{N_0}{Z_0(T)}\right) \end{aligned} \quad (5)$$

where the subscripts 1 and 2 represent the neutral and the ionic lines, respectively. m is the mass of the electron (kg), c is the

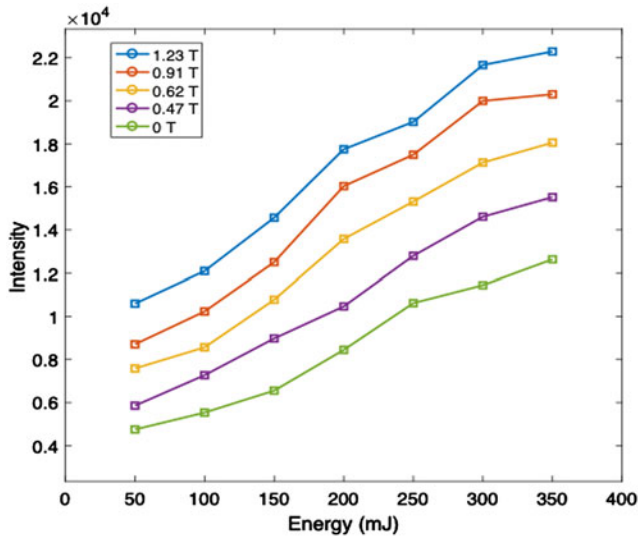


Fig. 19. A plot of the intensities of the Mg I-518.4 nm spectra line against the laser energies at the presence and absence of the magnetic field.

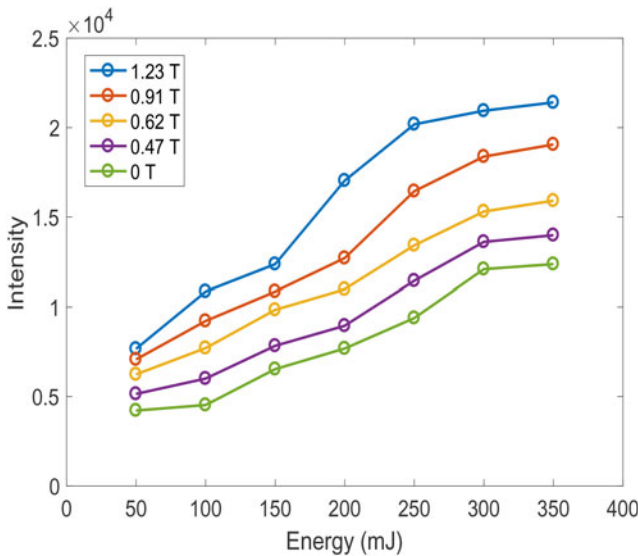


Fig. 20. A plot of the intensities of the Ti II-376.2 nm spectra line against the laser energies at the presence and absence of the magnetic field.

speed of light, $Z_0(T)$ denotes the partition function, E_{IP} is the ionization energy (eV), A is the transition probability, T is the plasma temperature (K), N_0 is the particle density of the element, and N_e is electron density (m^{-3}) (Griem, 1997; Gomba *et al.*, 2001; Duixiong *et al.*, 2014).

Equation (5) can be reduced to the Boltzmann plot equation by expressing the energies E_k^1 and $E_k^* = E_k^2 + E_{IP}$ for both the neutral and the ionic lines, respectively. We obtain a reduced form of Eq. (5) as follows:

$$\ln\left(\frac{I_1 \lambda_1}{g_1 A_1}\right)^* = -\frac{1}{kT} E_k^* + \ln\left(\frac{hc N_0}{Z_0(T)}\right) \quad (6)$$

From the Boltzmann plot, the electron temperatures of the Mg plasma at a delay time of 5 μs and a laser energy of 250 mJ

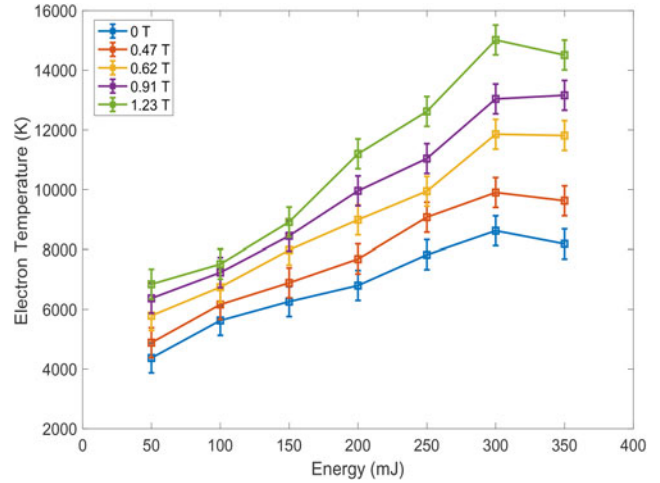


Fig. 21. A plot of electron temperature of Mg plasma against laser energy, with a delay time of 20 μs at the presence and absence of magnetic fields of 0, 0.47, 0.62, 0.91, and 1.23 T.

were found to be 7428, 9643, 11,038, and 12,618 K, which correspond to the magnetic fields of 0, 0.43, 0.62, and 0.91 T, respectively. From Figure 21, the electron temperature of the Mg plasma recorded its highest electron temperature of 14,591 K with a laser energy of 300 mJ and a delay time of 10 μs at the presence of a magnetic field of 1.23 T. The error bars in the figure show the standard deviations in calculating the electron temperatures.

The Saha-Boltzmann plot method was also used to determine the electron temperature of the Ti plasma. The slope of the plot gave an electron temperature of 6085, 7045, 8012, 9078, and 9987 K with a delay time of 5 μs at the presence and absence of magnetic fields of 0, 0.47, 0.62, 0.91, and 1.23 T, respectively. The highest electron temperature of the Ti plasma was recorded to be 15,720 K at a delay time of 10 μs . We also observe a sharp increase in the electron temperature with increasing laser energy at the presence of a magnetic field of 1.23 T. Figure 22 shows a plot of the electron temperature of Ti plasma against the laser energy, with a delay time of 20 μs .

Electron density

In this section, we further evaluate the electron density from the Stark broadening mechanism. The line profiles of the Mg and the Ti lines are fitted to the Lorentzian fit as depicted in Figure 16. The full width at half maximum of the spectral lines can be used to evaluate the electron number density by the relation (Sun *et al.*, 2013; Asamoah and Hongbing, 2017; Ghezlbash *et al.*, 2017):

$$\Delta\lambda_{1/2}(\text{nm}) = 2\omega\left(\frac{N_e}{10^{16}}\right) + 3.5 A\left(\frac{N_e}{10^{16}}\right)^{1/4} \left[1 - \frac{3}{4} N_D^{-1/3}\right] \omega\left(\frac{N_e}{10^{16}}\right) \quad (7)$$

where N_e is the electron density, A is the ionic broadening parameter (nm), ω is the electron impact width parameter (nm), and N_D denotes the number of particles in the Debye sphere. Neglecting the ionic broadening from Eq. (7), due to its

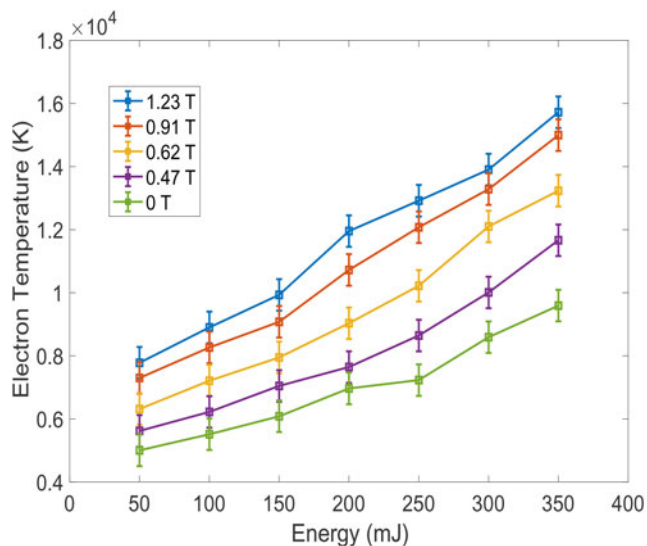


Fig. 22. A plot of electron temperature of Ti plasma against laser energy, with a delay time of 20 μs at the presence and absence of magnetic fields of 0, 0.47, 0.62, 0.91, and 1.23 T.

minor contribution to the broadening, hence, Eq. (7) can be reduced to the form:

$$\Delta\lambda_{1/2}(\text{nm}) = 2\omega\left(\frac{N_e}{10^{16}}\right) \quad (8)$$

Figures 23 and 24 show the plot of electron density against the laser energy of Mg and Ti, respectively, at the presence and absence of magnetic field. The electron density was deduced from the stark broadening at the presence and absence of the magnetic field. In the absence of the magnetic field, the electron density of the Mg plasma was found to be in the range from 1.03×10^{18} to $1.68 \times 10^{18} \text{ cm}^{-3}$ with varying laser energy from 50 to 350 mJ. At the presence of the magnetic fields of 0.47, 0.62, 0.91, and 1.23 T, the electron density was found to be in the range of 1.14×10^{18} – 1.81×10^{18} , 1.28×10^{18} – 1.92×10^{18} , 1.42×10^{18} – 2.03×10^{18} , and 1.55×10^{18} – $2.14 \times 10^{18} \text{ cm}^{-3}$, respectively, with varying laser energy from 50 to 350 mJ.

The electron density of the Ti plasma was found in the range of 0.97×10^{18} – $1.53 \times 10^{18} \text{ cm}^{-3}$ at the absence of the magnetic field. And with an applied magnetic field of 0.47, 0.62, 0.91, and 1.23 T, the electron densities of the Ti plasma were found to be in the range of 1.07×10^{18} – 1.65×10^{18} , 1.13×10^{18} – 1.72×10^{18} , 1.26×10^{18} – 1.83×10^{18} , and 1.33×10^{18} – $1.89 \times 10^{18} \text{ cm}^{-3}$, respectively.

We recorded an increasing trend of the electron density with an increasing magnetic field. The electron density shows that the energy transfer within the plasma plume and the collisions significantly increased with the applied magnetic field, hence increasing both the electron temperature and the electron density.

Validity of the LTE

For an accurate and precise analysis of the qualitative and quantitative study of the elemental composition of target samples, it is imperative to establish the validity of Local Thermodynamic Equilibrium (LTE) and also determine that the plasma of the sample is optically thin. Failure to warrant the existence of LTE

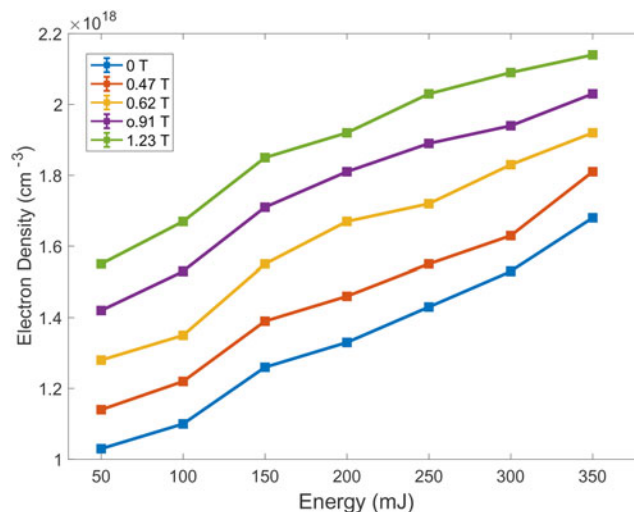


Fig. 23. A plot of electron density of Mg plasma against laser energy, with a delay time of 15 μs at the presence and absence of magnetic fields of 0, 0.47, 0.62, 0.91, and 1.23 T.

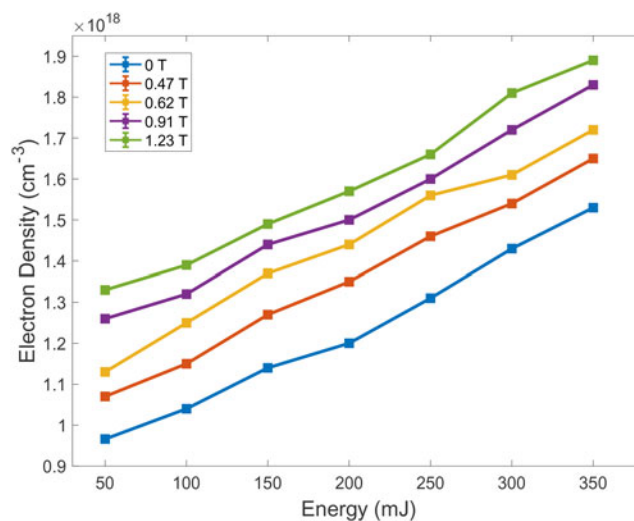


Fig. 24. A plot of electron density of Ti plasma against laser energy, with a delay time of 15 μs at the presence and absence of magnetic fields of 0, 0.47, 0.62, 0.91, and 1.23 T.

conditions might lead to incorrect and unreliable measurements as a result of intense self-absorption of the plasma.

McWhirter's criterion (Sabsabi and Cielo, 1995) should be fulfilled before LTE can be established. The criterion is based on the fact that the collision rate of the electrons should be more than that of the radiation rate. When this case happens, the plasma is classified to be in LTE. The criterion requires a certain amount of electron number density to be present for LTE to be ascertained, which can be expressed mathematically as follows (Aguilera and Aragón, 2004; Dawood and Bashir, 2018):

$$N_e \geq 1.6 \times 10^{12} T^{1/2} (\Delta E)^3 \quad (9)$$

where T is the plasma temperature (K) and ΔE is the energy difference between the transition levels of the upper and lower energy levels of both the Mg and Ti lines under investigation.

When the evaluated electron number density, from the experiment using the Stark broadening of the atomic and ionic lines, is higher than the electron number density estimated from the McWhirter's criterion, then we can establish that the plasma is said to be in LTE. Several research works have proved that McWhirter's criterion is not a sufficient method to ascertain the existence of LTE. From this work, we evaluated the electron density from the temperatures of the Mg and Ti plasmas, and the electron density was found to be in the order of 10^{18} cm^{-3} which was high enough to affirm the existence of LTE. Also, we established that the plasma was optically thin from the line intensities obtained and chosen for the calculation of the plasma temperatures.

Conclusion

The influence of cavity and magnetic confinement on the signal enhancement of laser-induced Mg and Ti plasmas generated by a Q-switched Nd:YAG laser is studied. The circular and square cavities were used to confine the plasma plume. We found that there was a significant enhancement in the spectral intensities of the three different circular cavity radii as compared with the cavity-free case. The maximum enhancement factor of the Mg I-518.4 nm line was reached at approximately 3.8, 3.4, and 2.8 at a delay time of 350 ns and a laser energy of 350 mJ for circular cavities of radii 2.5, 3.0, and 3.5 mm, respectively. Comparing the circular cavity of radius 3.5 mm with the square cavity at a delay time of 300 ns and a laser energy of 300 mJ, the intensity of the circular cavity was more enhanced as compared to the square cavity. The value for the electron temperature for the cavity-free case (without cavity) was found to be 7423 K at a delay time of 200 ns and a laser energy of 300 mJ. With the same experimental conditions, the electron temperature of the circular cavities of radii 2.5, 3.0, and 3.5 mm was recorded at 9188, 8575, and 7683 K, respectively. At the presence of the magnetic field, we also observed a tremendous effect on the electron temperature and density. The value of the electron temperatures of Mg and Ti plasmas recorded their highest electron temperatures of 14,591 and 15,720 K with a laser energy of 300 mJ and a delay time of 10 μs at the presence of magnetic field of 1.23 T. Varying the magnetic field from 0.47 to 1.23 T, the temperature of the plasma increased significantly, and this was attributed to the adiabatic compression and Joule heating. The electron density of Mg and Ti plasmas at the presence of the magnetic field of 1.23 T was found to be in the range of 1.55×10^{18} – 2.14×10^{18} and 1.33×10^{18} – $1.89 \times 10^{18} \text{ cm}^{-3}$, respectively. From our calculations, the value of β , which was less than 1 for all the cases, confirms that there was a plasma confinement at the presence of the magnetic field.

Acknowledgments. This work was supported by the National Natural Science Foundation of China (Nos. 51775253 and 61505071), the Fundamental Research Funds for the Central Universities (No. 2019B02614), and China Postdoctoral Science Foundation (2017M611725).

References

- Aguilera JA and Aragón C (2004) Characterization of a laser-induced plasma by spatially resolved spectroscopy of neutral atom and ion emissions: comparison of local and spatially integrated measurements. *Spectrochimica Acta Part B: Atomic Spectroscopy* **59**, 1861–1876.
- Ahmed N, Abdullah M, Ahmed R, Piracha NK and Baig MA (2017) Quantitative analysis of a brass alloy using CF-LIBS and a laser ablation time-of-flight mass spectrometer. *Laser Physics* **28**, 016002.
- Akhtar M, Jabbar A, Ahmed N, Mehmood S, Umar Z, Ahmed R and Baig M (2019) Magnetic field-induced signal enhancement in laser-produced lead plasma. *Laser and Particle Beams* **37**, 67–78.
- Amoruso S, Bruzzese R, Spinelli N and Velotta R (1999) Characterization of laser-ablation plasmas. *Journal of Physics B: Atomic, Molecular and Optical Physics* **32**, R131.
- Asamoah E and Hongbing Y (2017) Influence of laser energy on the electron temperature of a laser-induced Mg plasma. *Applied Physics B* **123**, 22.
- Asimellis G, Hamilton S, Giannoudakos A and Kompitsas M (2005) Controlled inert gas environment for enhanced chlorine and fluorine detection in the visible and near-infrared by laser-induced breakdown spectroscopy. *Spectrochimica Acta Part B: Atomic Spectroscopy* **60**, 1132–1139.
- Awan MA, Ahmed SH, Aslam MR, Qazi IA and Baig MA (2013) Determination of heavy metals in ambient air particulate matter using laser-induced breakdown spectroscopy. *Arabian Journal for Science and Engineering* **38**, 1655–1661.
- Bashir S, Farid N, Mahmood K and Rafique MS (2012) Influence of ambient gas and its pressure on the laser-induced breakdown spectroscopy and the surface morphology of laser-ablated Cd. *Applied Physics A* **107**, 203–212.
- Boueri M, Motto-Ros V, Lei W-Q, Zheng L-J and Zeng H-P (2011) Identification of polymer materials using laser-induced breakdown spectroscopy combined with artificial neural networks. *Applied Spectroscopy* **65**, 307–314.
- Bridge CM, Powell J, Steele KL and Sigman ME (2007) Forensic comparative glass analysis by laser-induced breakdown spectroscopy. *Spectrochimica Acta Part B: Atomic Spectroscopy* **62**, 1419–1425.
- Carmona N, Oujja M, Rebollar E, Römich H and Castillejo M (2005) Analysis of corroded glasses by laser induced breakdown spectroscopy. *Spectrochimica Acta Part B: Atomic Spectroscopy* **60**, 1155–1162.
- Choi J-J, Choi S-J and Yoh JJ (2016) Standoff detection of geological samples of metal, rock, and soil at low pressures using laser-induced breakdown spectroscopy. *Applied Spectroscopy* **70**, 1411–1419.
- Corsi M, Palleschi V, Salvetti A and Tognoni E (2002) Calibration free laser induced plasma spectroscopy: a new method for combustion products analysis. *Clean Air* **3**, 69–79.
- Cremers DA and Radziemski LJ (1983) Detection of chlorine and fluorine in air by laser-induced breakdown spectrometry. *Analytical Chemistry* **55**, 1252–1256.
- Dawood A and Bashir S (2018) Characterizing laser induced plasma and ablation of Mg-alloy in the presence and absence of magnetic field. *Optik* **170**, 353–367.
- Dawood A, Bashir S, Chishti NA, Khan MA and Hayat A (2018) Magnetic field effect on plasma parameters and surface modification of laser-irradiated Cu-alloy. *Laser and Particle Beams* **36**, 261–275.
- Duixiong S, Maogen S, Chenzhong D and Guan hong W (2014) A comparative study of the laser induced breakdown spectroscopy in single-and collinear double-pulse laser geometry. *Plasma Science and Technology* **16**, 374.
- Gao X, Liu L, Song C and Lin J (2015) The role of spatial confinement on nanosecond YAG laser-induced Cu plasma. *Journal of Physics D: Applied Physics* **48**, 175205.
- Ghezlbash M, Majd AE, Darbani SMR and Ghasemi A (2017) Experimental investigation of atomic and ionic titanium lines, diatomic TiO_y transition and continuum background radiation via magnetically confined LIBS. *Ceramics International* **43**, 8356–8363.
- Giakoumaki A, Melessanaki K and Anglos D (2007) Laser-induced breakdown spectroscopy (LIBS) in archaeological science—applications and prospects. *Analytical and Bioanalytical Chemistry* **387**, 749–760.
- Gomba J, D'Angelo C, Bertuccelli D and Bertuccelli G (2001) Spectroscopic characterization of laser induced breakdown in aluminium–lithium alloy samples for quantitative determination of traces. *Spectrochimica Acta Part B: Atomic Spectroscopy* **56**, 695–705.
- Gottfried JL, De Lucia Jr FC, Munson CA and Miziolek AW (2008) Strategies for residue explosives detection using laser-induced breakdown spectroscopy. *Journal of Analytical Atomic Spectrometry* **23**, 205–216.
- Griem H (1997) *Principles of Plasma Spectroscopy*. Cambridge: Cambridge University.
- Guo L, Hu W, Zhang B, He X, Li C, Zhou Y, Cai Z, Zeng X and Lu Y (2011) Enhancement of optical emission from laser-induced plasmas by combined spatial and magnetic confinement. *Optics Express* **19**, 14067–14075.

- Guo L, Hao Z, Shen M, Xiong W, He X, Xie Z, Gao M, Li X, Zeng X and Lu Y (2013) Accuracy improvement of quantitative analysis by spatial confinement in laser-induced breakdown spectroscopy. *Optics Express* **21**, 18188–18195.
- Harilal S, Tillack M, O'shay B, Bindhu C and Najmabadi F (2004) Confinement and dynamics of laser-produced plasma expanding across a transverse magnetic field. *Physical Review E* **69**, 026413.
- Harmon RS, DeLucia FC, McManus CE, McMillan NJ, Jenkins TF, Walsh ME and Miziolek A (2006) Laser-induced breakdown spectroscopy: an emerging chemical sensor technology for real-time field-portable, geochemical, mineralogical, and environmental applications. *Applied Geochemistry* **21**, 730–747.
- Hongbing Y, Asamoah E, Jiawei C, Dongqing Y and Fengxiao Y (2018) Comprehensive study on the electron temperature and electron density of laser-induced Mg plasma. *Journal of Lasers, Optics and Photonics* **5**, 181.
- Iftikhar H, Bashir S, Dawood A, Akram M, Hayat A, Mahmood K, Zaheer A, Amin S and Murtaza F (2017) Magnetic field effect on laser-induced breakdown spectroscopy and surface modifications of germanium at various fluences. *Laser and Particle Beams* **35**, 159–169.
- Joshi H, Kumar A, Singh R and Prahlad V (2010) Effect of a transverse magnetic field on the plume emission in laser-produced plasma: an atomic analysis. *Spectrochimica Acta Part B: Atomic Spectroscopy* **65**, 415–419.
- Lee Y, Song K and Sneddon J (1997) *Laser Induced Plasmas for Analytical Atomic Spectroscopy*. New York, NY: Wiley-VCH.
- Lei W, Motto-Ros V, Boueri M, Ma Q, Zhang D, Zheng L, Zeng H and Yu J (2009) Time-resolved characterization of laser-induced plasma from fresh potatoes. *Spectrochimica Acta Part B: Atomic Spectroscopy* **64**, 891–898.
- Li Y, Tian D, Ding Y, Yang G, Liu K, Wang C and Han X (2018) A review of laser-induced breakdown spectroscopy signal enhancement. *Applied Spectroscopy Reviews* **53**, 1–35.
- Markiewicz-Keszcyka M, Casado-Gavalda MP, Cama-Moncunill X, Cama-Moncunill R, Dixit Y, Cullen PJ and Sullivan C (2018) Laser-induced breakdown spectroscopy (LIBS) for rapid analysis of ash, potassium and magnesium in gluten free flours. *Food Chemistry* **244**, 324–330.
- Michel AP, Lawrence-Snyder M, Angel SM and Chave AD (2007) Laser-induced breakdown spectroscopy of bulk aqueous solutions at oceanic pressures: evaluation of key measurement parameters. *Applied Optics* **46**, 2507–2515.
- Müller K and Stege H (2003) Evaluation of the analytical potential of laser-induced breakdown spectrometry (LIBS) for the analysis of historical glasses. *Archaeometry* **45**, 421–433.
- Naes BE, Umpierrez S, Ryland S, Barnett C and Almirall JR (2008) A comparison of laser ablation inductively coupled plasma mass spectrometry, micro X-ray fluorescence spectroscopy, and laser induced breakdown spectroscopy for the discrimination of automotive glass. *Spectrochimica Acta Part B: Atomic Spectroscopy* **63**, 1145–1150.
- Neogi A and Thareja R (1999) Laser-produced carbon plasma expanding in vacuum, low pressure ambient gas and nonuniform magnetic field. *Physics of Plasmas* **6**, 365–371.
- NIST Atomic spectra database. Available at: http://Physics.nist.gov/PhysRef-Data/ASD/lines_form.html
- Popov AM, Colao F and Fantoni R (2009) Enhancement of LIBS signal by spatially confining the laser-induced plasma. *Journal of Analytical Atomic Spectrometry* **24**, 602–604.
- Popov AM, Labutin TA, Zaytsev SM, Seliverstova IV, Zorov NB, Kal'ko IA, Sidorina YN, Bugaev IA and Nikolaev YN (2014) Determination of Ag, Cu, Mo and Pb in soils and ores by laser-induced breakdown spectrometry. *Journal of Analytical Atomic Spectrometry* **29**, 1925–1933.
- Radziemski LJ and Cremers DA (1989) *Laser-induced Plasmas and Applications*. Marcel Dekker Inc, New York.
- Rai V, Shukla M and Pant H (1998) Some studies on picosecond laser produced plasma expanding across a uniform external magnetic field. *Laser and Particle Beams* **16**, 431–443.
- Rodriguez-Celis E, Gornushkin I, Heitmann U, Almirall J, Smith B, Winefordner J and Omenetto N (2008) Laser induced breakdown spectroscopy as a tool for discrimination of glass for forensic applications. *Analytical and Bioanalytical Chemistry* **391**, 1961.
- Sabsabi M and Cielo P (1995) Quantitative analysis of aluminum alloys 14058-8 by laser-induced breakdown spectroscopy and plasma characterization. *Applied Spectroscopy* **49**, 499–507.
- Shaheen N, Irfan NM, Khan IN, Islam S, Islam MS and Ahmed MK (2016) Presence of heavy metals in fruits and vegetables: health risk implications in Bangladesh. *Chemosphere* **152**, 431–438.
- Shao J, Wang T, Guo J, Chen A and Jin M (2017) Effect of cylindrical cavity height on laser-induced breakdown spectroscopy with spatial confinement. *Plasma Science and Technology* **19**, 025506.
- Shen X, Lu Y, Gebre AT, Ling H and Han Y (2006) Optical emission in magnetically confined laser-induced breakdown spectroscopy. *Journal of Applied Physics* **100**, 053303.
- Sturm V and Noll R (2003) Laser-induced breakdown spectroscopy of gas mixtures of air, CO₂, N₂, and C₃H₈ for simultaneous C, H, O, and N measurement. *Applied Optics* **42**, 6221–6225.
- Sturm V, Peter L and Noll R (2000) Steel analysis with laser-induced breakdown spectrometry in the vacuum ultraviolet. *Applied Spectroscopy* **54**, 1275–1278.
- Sun D, Su M, Dong C, Wen G and Cao X (2013) A comparative study of the laser induce breakdown spectroscopy in single-and double-pulse laser geometry.
- Sun Y, Zhong S, Lu Y, Sun X, Ma J and Liu Z (2015) Application of LIBS in element analysis of nanometer thin film prepared on silicon basement. *Guang pu xue yu guang pu fen xi* **35**, 1376–1382.
- Wang Q, Chen A, Zhang D, Wang Y, Sui L, Li S, Jiang Y and Jin M (2018) The role of cavity shape on spatially confined laser-induced breakdown spectroscopy. *Physics of Plasmas* **25**, 073301.
- Zhang H, Yueh F-Y and Singh JP (1999) Laser-induced breakdown spectrometry as a multimetal continuous-emission monitor. *Applied Optics* **38**, 1459–1466.
- Zhang S, Wang X, He M, Jiang Y, Zhang B, Hang W and Huang B (2014) Laser-induced plasma temperature. *Spectrochimica Acta Part B: Atomic Spectroscopy* **97**, 13–33.